
AFRL-AFOSR-JP-TR-2018-0065

# Development of Advanced Li Rich xLi2MO3-(1-x)LiMO2 Composite Cathode for High Capacity Li Ion Batteries

**Ying Shirley Meng**
**UNIVERSITY OF CALIFORNIA SAN DIEGO**

**08/14/2018**
**Final Report**

**DISTRIBUTION A: Distribution approved for public release.**

Air Force Research Laboratory
AF Office Of Scientific Research (AFOSR)/ IOA
Arlington, Virginia 22203
Air Force Materiel Command

DISTRIBUTION A: Distribution approved for public release

# REPORT DOCUMENTATION PAGE

*Form Approved*
*OMB No. 0704-0188*

**The public reporting burden for this collection of information is estimated to average 1 hour per response, including the time for reviewing instructions, searching existing data sources, gathering and maintaining the data needed, and completing and reviewing the collection of information. Send comments regarding this burden estimate or any other aspect of this collection of information, including suggestions for reducing the burden, to Department of Defense, Executive Services, Directorate (0704-0188). Respondents should be aware that notwithstanding any other provision of law, no person shall be subject to any penalty for failing to comply with a collection of information if it does not display a currently valid OMB control number.**
**PLEASE DO NOT RETURN YOUR FORM TO THE ABOVE ORGANIZATION.**

| 1. REPORT DATE *(DD-MM-YYYY)* | 2. REPORT TYPE | 3. DATES COVERED *(From - To)* |
|---|---|---|
| 30-08-2018 | Final | 28 Sep 2015 to 27 May 2018 |

**4. TITLE AND SUBTITLE**
Development of Advanced Li Rich xLi2MO3-(1-x)LiMO2 Composite Cathode for High Capacity Li Ion Batteries

**5a. CONTRACT NUMBER**

**5b. GRANT NUMBER**
FA2386-15-1-4110

**5c. PROGRAM ELEMENT NUMBER**
61102F

**6. AUTHOR(S)**
Ying Shirley Meng

**5d. PROJECT NUMBER**

**5e. TASK NUMBER**

**5f. WORK UNIT NUMBER**

**7. PERFORMING ORGANIZATION NAME(S) AND ADDRESS(ES)**
UNIVERSITY OF CALIFORNIA SAN DIEGO
9500 GILMAN DR DEPT 621, OFFICE OF CONTRACT & GRANT ADMIN. 09
LA JOLLA, CA 92093-0621 US

**8. PERFORMING ORGANIZATION REPORT NUMBER**

**9. SPONSORING/MONITORING AGENCY NAME(S) AND ADDRESS(ES)**
AOARD
UNIT 45002
APO AP 96338-5002

**10. SPONSOR/MONITOR'S ACRONYM(S)**
AFRL/AFOSR IOA

**11. SPONSOR/MONITOR'S REPORT NUMBER(S)**
AFRL-AFOSR-JP-TR-2018-0065

**12. DISTRIBUTION/AVAILABILITY STATEMENT**
A DISTRIBUTION UNLIMITED: PB Public Release

**13. SUPPLEMENTARY NOTES**

**14. ABSTRACT**
Li-rich layered oxides (LRLO) composite cathode materials were studied with the goal of improving energy density with three main thrusts: computational modeling of cation substitution for stabilize oxygen, (2) exploration of coatings for improved capacity retention, and (3) mesostructural modification to improve cycling performance and rate capability. Computational modelling using density functional theory predicts 4d transition metals Mo and Ru to improve oxygen stability; experimental doping results were commensurate with calculation results, with Mo showed improved capacity retention and reduced oxygen evolution. LLTO coating was demonstrated to improve capacity retention by preventing surface reconstruction, as evident by high resolution STEM. Mesostructure modification was explored through varied processing method, showing a high degree of particle tenability through precise processing control; such altered nanostructuring of secondary particles was shown to have a notable influence on particle cyclability. Great progress was made to determine causes of structural instability and to mitigate such instabilities in LRLO. Doping of a model layered Li-rich nickel manganese material was investigated via DFT calculations to explore stabilization of oxygen ions in the material, and guided by results, experimental doping and characterization was performed. The theoretical model was validated, as compared to previously published work on the evolution of oxygen vacancies. Of all dopants simulated, Mo and Ru were shown to increase the oxygen vacancy formation energy, EFOv, elucidating the potential to reduce oxygen evolution during cycling and improving overall capacity retention. This improved EFOv was attributed to a delocalization of the Mo electrons to the surrounding anions, serving to stabilize the oxygen ions by creating a larger barrier for charge transfer.

**15. SUBJECT TERMS**
Batteries, Electrodes, Cathodes, Composites, Lithium, Energy, Mesoporous, Failure Mechanism, Modeling, Oxygen Vacancy



DISTRIBUTION A: Distribution approved for public release

| 16. SECURITY CLASSIFICATION OF: | | | 17. LIMITATION OF ABSTRACT | 18. NUMBER OF PAGES | 19a. NAME OF RESPONSIBLE PERSON |
|---|---|---|---|---|---|
| a. REPORT | b. ABSTRACT | c. THIS PAGE | | | WINDER, SHEENA |
| Unclassified | Unclassified | Unclassified | SAR | | 19b. TELEPHONE NUMBER *(Include area code)* +81-42-511-2008 |

Standard Form 298 (Rev. 8/98)
Prescribed by ANSI Std. Z39.18

DISTRIBUTION A: Distribution approved for public release

Final Report for AOARD Grant FA2386-15-1-4110

"**Development of advanced Li-rich $xLi_2MO_3$-(1-x)$LiMO_2$ composite cathode for Li ion batteries with high energy density**"

**August 15, 2018**

**Name of Principal Investigators (PI and Co-PIs):**

- e-mail address : shirleymeng@ucsd.edu
- Institution : University of California, San Diego
- Mailing Address : 9500 Gilman Dr., Mail Code 0448, La Jolla, CA 92093
- Phone : 858-822-4247
- Fax : 858-534-9553

Period of Performance: 09/28/2015 – 05/27/2018
Program Officer: Dr. Sheena Winder

**Abstract:** Li-rich layered oxide (LRLO) composite cathode materials were studied with the goal of improving energy density with three main thrusts: computational modeling of cation substitution for stabilize oxygen, (2) exploration of coatings for improved capacity retention, and (3) mesostructural modification to improve cycling performance and rate capability. Computational modelling using density functional theory predicts 4d transition metals Mo and Ru to improve oxygen stability; experimental doping results were commensurate with calculation results, with Mo showed improved capacity retention and reduced oxygen evolution. LLTO coating was demonstrated to improve capacity retention by preventing surface reconstruction, as evident by high resolution scanning transmission electron microscopy. Mesostructure modification was explored through varied processing method, showing a high degree of particle tunability through precise processing control; such altered nanostructuring of secondary particles was shown to have a notable influence on particle cyclability.

**Introduction:**

Driven by the desire for longer lasting portable devices, lithium ion batteries have dominated the energy storage market due to their high energy densities.[1] The need for high energy density batteries has been further pushed by the emergence of the electric vehicle market—so much so that nearly all modern car manufacturers are striving to develop such technology. However, modern cathode materials are currently at a bottleneck for capacity, with the practical capacity of $LiCoO_2$ around 160 mAh/g).[2] Such commercial materials generally accommodate lithium shuttling through cationic redox reactions. Though a relatively young class of materials, lithium-rich layered oxides (LRLO) have recently shown capacities in excess of 300 mAh/g. These materials gain their name from the substitution of lithium into the transition metal layer. Uniquely, the increased capacity of LRLO has been attributed to redox of the oxygen anions—a truly novel phenomenon. However, despite nearly two decades of research, LRLO are still far from a commercially viable state. Primarily, these materials suffer from high degrees of voltage fade and capacity loss—mechanisms recently shown to be attributed to the dynamic evolution of a variety of defects throughout the material.[3,4] Earlier work identified the surface as undergoing a transition from layered to spinel-like, facilitated by oxygen ion migration, attributed to capacity loss and limited rate capability.[5] Similarly, recent application of Bragg coherent diffractive imaging (BCDI), has uncovered the dynamic evolution of dislocation networks and microstrain within the structure, though these defects, as well as the voltage profile, were shown to be recoverable with a mild heat treatment of 180 °C.[4]

One common theme is present in the role of oxygen evolution in LRLO: loss of oxygen from the structure may result in enhanced structural degradation by facilitating transition metal migration as well as reducing the amount of oxygen available to undergo redox. With this consideration in mind, the goal of this work was to take a multifaced approach to push forward the current state of LRLO: (1) to apply computational modeling to determine the impact of cation substitution on the stability of oxygen within the bulk layered lithium rich structure, (2) to evaluate the impact of structural modification on capacity fade, and (3) to through surface treatment and nanostructuring of cathode



DISTRIBUTION A: Distribution approved for public release

materials.

## 1. Theoretically designed cation substitution on oxygen stability

### Introduction and goals

Oxygen loss in LRLO is known to contribute to its rapid degradation in the form of reduced structural stability and further loss of capacity. Previous methodologies have focused on surface modification to reduce oxygen loss through modified oxygen concentration gradients, while largely ignoring the bulk as a source of large-scale degradation. Recent results have shown large degrees of internal defects present, which are coupled experimentally with reduced capacity and the notable voltage fade.[4] Methods to stabilize bulk effects are limited, though doping or cation substitution has proven useful in improving long-term performance of many cathode materials; for example, with only 5 at% aluminum in the transition metal layer, NCA has become a mainstream cathode material for commercial applications.

However, rational design of such materials is crucial for both speed of materials development and efficient use of resources. Application of Density Functional Theory (DFT) for large-scale predictive testing has become a standard for many aspects of research, streamlining experimental design and predicting a range of behaviors including enhanced ionic conductivity[6] and decomposition of solid state interfaces.[7] Here, DFT modeling of cationic substitution is performed with the goal of improving bulk oxygen stability, aiming to improve cyclability of LRLO through stabilization of oxygen anions while leaving oxygen available to participate in redox. Based on results of the simulations, experimental doping is performed to verify the predicted behavior.

Theoretical model and implications

A spin-polarized GGA+*U* approximation to the Density Functional Theory (DFT) was employed, to account for electron correlations in transition metal and rare earth elements. Projector augmented-wave method (PAW) pseudopotentials were used as implemented in the Vienna Ab Initio Simulation Package (VASP). The Perdew-Burke-Ernzerhof exchange correlation and a plane wave representation for the wavefunction with a cutoff energy of 450 eV were used. The Brillouin zone was sampled with a k-points mesh of 5 x 4 x 7 for structural relaxations and oxygen vacancy formation energy calculations and 10 x 8 x 14 for density of states (DOS) calculations, both by Gamma packing. Atomic coordinates and lattice vectors were fully relaxed for each structure. Effective *U* values used in the calculations are shown in Table 1.1, with the rotationally invariant approach (fixed *J*=1).[8]

**Table 1.1:** Effective *U* values used in GGA+*U* calculations[9–18].

| Co | Fe | Mo | Mn | Nb | Ni | Ru | Sc | Ti | V | Y | Zr |
|---|---|---|---|---|---|---|---|---|---|---|---|
| 4.91[9] | 4.3[9] | 2.5[10] | 6.96[11] | 2.07[12] | 6[11] | 3[13] | 6[14] | 4.2[15] | 4[16] | 5.08[17] | 2[18] |

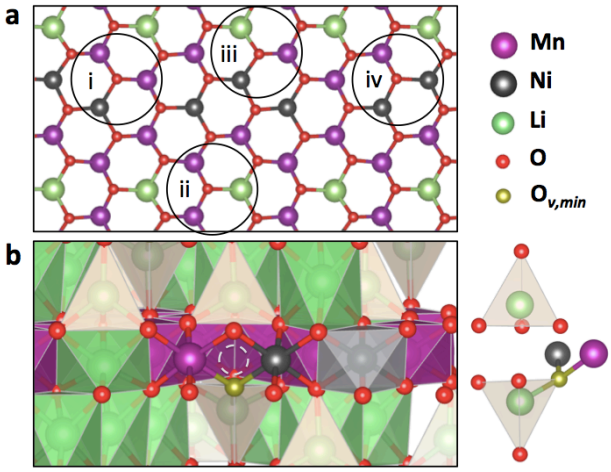


**Figure 1.1:** (a) The most stable arrangement of transition metals within the transition metal layer, demonstrating four different local bonding environments surrounding oxygen ions. (b) The relaxed



DISTRIBUTION A: Distribution approved for public release

structure at a lithiation state of 8/14 exhibits the formation of a lithium dumbbell, observed to be a common factor in the lowest oxygen vacancy formation energy site.

An undoped model supercell composed of twelve formula units of $Li[Li_{2/12}Ni_{3/12}Mn_{7/12}]O_2$ with the $R\bar{3}m$ layered structure was used to simulate the Li-rich material, shown in Figure 1.1. The undoped supercell was calculated for all possible in-plane transition metal layer configurations, which showed lithium ions surrounded by 6 Mn ions or 5 Mn and 1 Ni ions in plane. This stable structure was then doped, replacing one manganese ion with one dopant ion, creating the formula unit $Li[Li_{2/12}Ni_{3/12}Mn_{6/12}M_{1/12}]O_2$, where M is the dopant. Of the 7 possible local bonding environments, the lowest energy dopant site was used for oxygen vacancy formation energy calculations.

To validate the un-doped computational method described, data was compared to previously published work by Qian, et al.[5] This prior work calculated the impact of delithiation on the oxygen vacancy formation energy of the same undoped structure used in this study. The initial structural model shows similar results with respect to structure and oxidation state changes. In both models nickel is oxidized, and the manganese oxidation state remains static. The oxygen vacancy formation energy was calculated by the following equation:

$$E_f = E\left(Li_{x/12}Ni_{1/4}Mn_{7/12}O_{2-y/12}\right) + \frac{y}{24}E(O_2) - E\left(Li_{\frac{x}{12}}Ni_{\frac{1}{4}}Mn_{\frac{7}{12}}O_2\right) - 1.36$$

where $E_{Ov}^{F}$ is the oxygen vacancy formation energy, $E(O_2)$ is the binding energy of molecular oxygen, and the -1.36 eV is an $O_2$ binding error correction for GGA+$U$ calculations.[19]

To verify the potential for oxygen redox within the material, a closer look at the density of states surrounding various oxygen ions was performed. Recent work by Seo, et al.[20] suggest the presence of a linear Li-O-Li bond produces a labile state for oxygen electrons, making these anions susceptible to oxidation. While such an analysis had been performed on single cation systems, little care has been taken in literature to investigate the local density of states, or those in the immediate environment of particular oxygen ions. Figure 1.2b suggests that the GGA+$U$ methodologies adequately describe the non-bonding orbitals to the extent proposed by Seo, et al., with a notably increased density of states on oxygen ions directly below the Fermi level. We further note that this phenomena is most clear in cases with a Ni nearest neighbor. However, further computational literature[21] has suggested that this metric of high electron occupation on oxygen below the Fermi level is not sufficient, and these electrons must exhibit a degree of overlap in antibonding levels. Application of the LOBSTER code (Local-Orbital Basis Suite Towards Electronic-Structure Reconstruction) further verifies this to be the case, with a high antibonding (negative) population overlap at a similar location to the increased oxygen density of states, confirming the applicability of the model structure and creating the potential to analyze oxygen redox activity using DFT.

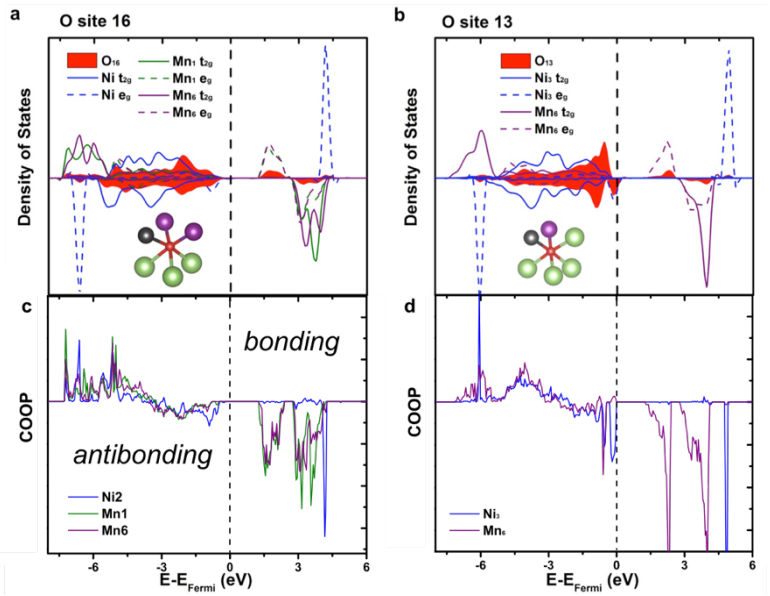


**Figure 1.2:** An example of the density of states (a,b) and COOP (c,d) population oxygen site in the fully lithiated structure (a,c) without a Li-O-Li linear bond and (b,d) with a Li-O-Li linear bond,



DISTRIBUTION A: Distribution approved for public release

required for labile oxygen states. The presence of the Li-O-Li linear configuration shows a greatly increased 2p density of states within 1.5 eV of the Fermi energy, and similarly large antibonding orbital overlap below the Fermi energy.

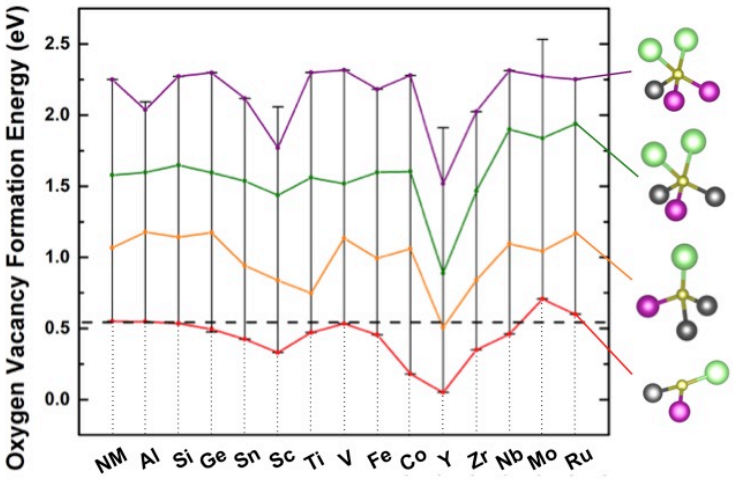


**Figure 1.3:** Calculated oxygen vacancy formation energies for the delithiated case of 8/14 Li concentration for the full range of doped materials. Trend lines relate the oxygen vacancy formation energy with the local bonding environment.

Now attention is drawn to the undoped, delithiated structure, shown in Figure 1.1b. Upon delithiation to a 8/14 lithium concentration, it is observed that lithium relaxes to the tetrahedral sites above and below a lithium vacancy in the transition metal layer. This occupation is referred to as a dumbbell configuration, and leads to the least stable oxygen configuration. Each of the oxygen ions surrounding this vacancy and tetrahedral occupancy shows a severely reduced $E_{Ov}^{F}$. Further, a range of $E_{Ov}^{F}$ is observed, as illustrated in Figure 1.3. The range in $E_{Ov}^{F}$ is attributed to three critical environmental factors: (1) the presence of a Ni nearest neighbors generally results in a lower oxygen vacancy formation energy, due to reduced electrostatic repulsion between the oxygen vacancy (effectively a positive charge) and the less positive Ni cation; (2) a minimized coordination with cations; and (3) subsequently occurs near a TM layer lithium vacancy and hence is in proximity to a tetrahedral lithium ion.

The impact of doping on the $E_{Ov}^{F}$ can be seen in Figure 1.3. Notable observations from this figure include the energy range of $E_{Ov}^{F}$ observed, and the relative changes in the $E_{Ov,min}^{F}$ with dopant incorporation. Of the tested dopants, only two had shown improved oxygen stability upon delithiation, which would potentially suppress oxygen evolution during cycling of the Li-rich material. These

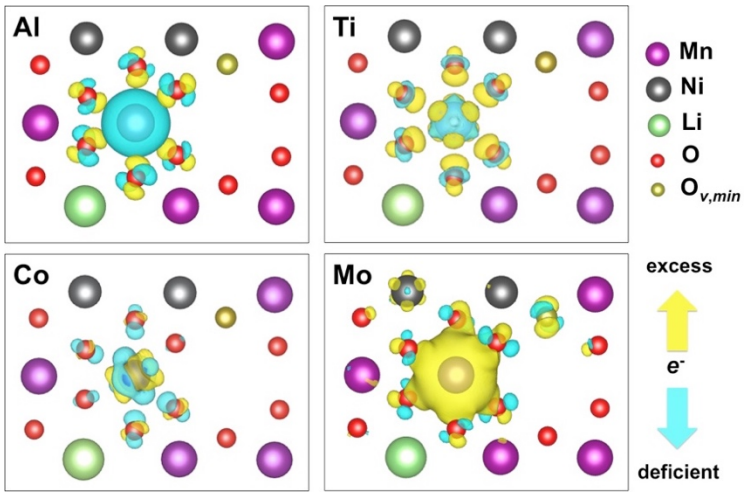




DISTRIBUTION A: Distribution approved for public release

**Figure 1.4:** Difference in charge density surrounding the dopant ion and local environment. Despite the modified charge density surrounding Al, Ti, and Co dopants, the reach of modified charge density does not extend beyond the immediate octahedron. In the case of Mo-doped material, electron density extends beyond the nearest neighbors, stabilizing the most unstable oxygen ions in proximity.

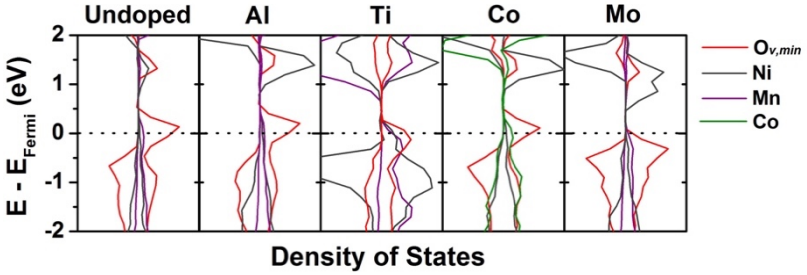


**Figure 1.5:** Projected density of states of the least stable oxygen ion and the nearest cations show Mo-doped material stabilizes the least stable oxygen ion by shifting bonding levels beneath the Fermi energy.

included molybdenum and ruthenium (to a lesser extent), both of which are 4d transition metals; due to ruthenium's high cost, it is not further considered in the remainder of the analysis. Other dopants either made no difference or decreased the barrier to oxygen vacancy formation. Further computational analysis was then limited to common dopants including aluminum and titanium (having no impact on oxygen stability), and cobalt (shown to reduce oxygen stability), and molybdenum to explore its improved oxygen stability.

To better understand the source of modified $E_{Ov}^{F}$, charge density differences were calculated (Figure 1.4). For clarity, charge density differences between undoped and doped structures were calculated for the same dopant site, and in the case of Co will not reflect the exact bonding environment present in the minimum $E_{Ov}^{F}$ value. However, for the intent of observing change in charge distribution, the simulation yields fundamentally applicable results. The presence of Al shows a relative decrease in local charge density, and modified oxygen occupation occurs due to coulombic effects. Cobalt and titanium show modified bonding behavior associated with the change in orbital occupation, yet the modified charge density does not extend to the most volatile oxygen site. Mo-doping on the other hand, shows an excess charge density, which extends beyond the immediately local oxygen ions, to the volatile oxygen site, serving to stabilize the oxygen. This effect is similarly observed in an analysis of the projected density of states on the least stable oxygen ion (Figure 1.5); the increased charge density is reflected in the downward energy shift of the oxygen 2p orbitals below the Fermi energy. This would serve as an impediment to charge transfer of the anions valence electrons, required for the release of an oxygen ion.

Further explanation of the modified charge density on oxygen ions for the case of Mo-doping may be derived from the impact of strain modification. The majority of the material maintains the theoretical bond lengths of the undoped material. However, when large ions are incorporated, these ions locally experience a compressive strain in the out-of-plane direction, while the original TM ions exhibit a tensile strain out-of-plane. Such tensile strain distorts the octahedra, modifying crystal field splitting, potentially accounting for the modified charge density observed. Analyses of the magnetic moments of valence electrons on the transition metals elucidate the oxidation state and electron configuration of the transition metal ions. This data describes the oxidation/reduction of the transition metals accompanying lithium removal/insertion. Table  describes the changes in oxidation state predicted by the magnetization data. Elements not listed in the table do not undergo a change of oxidation state. The magnetization data calculated from the undoped case matches with previous work, showing a static magnetic moment on Mn ions, and a decreasing magnetic moment with delithiation for Ni ions.[3] To reiterate, $Mn^{4+}$ maintains its valence, where Ni oxidizes from 2+/3+ to 3+/4+ with delithiation. Though aluminum doping did not significantly alter $E_{Ov}^{F}$, nickel redox is changed such that one nickel ion begins as $Ni^{3+}$. Molybdenum doping showed a more significant change, with one of the manganese ions beginning in a 3+ valence state and undergoing oxidation with delithiation (3+/4+), and one Ni not showing redox behavior at this lithiation state. Last, magnetic moments show that molybdenum undergoes redox (5+/6+); this redox was compensated by the aforementioned $Mn^{3+}$ ion.



DISTRIBUTION A: Distribution approved for public release

**Table 1.3**: Oxidation state change on charging (from 14/14 to 8/14 Li concentration) was determined by observing magnetic moments at the different states of charge. Elements not included in the table below did not undergo an oxidation state change. The multiplier at right indicates the number of elements in the supercell showing that particular oxidation state change.

| Dopant | Theor. Redox change | |
|---|---|---|
| No dopant | $Ni^{2+} \rightarrow Ni^{3+}$ | x 2 |
| | $Ni^{2+} \rightarrow Ni^{4+}$ | x 1 |
| Al | $Ni^{2+} \rightarrow Ni^{3+}$ | x 2 |
| | $Ni^{2+} \rightarrow Ni^{4+}$ | x 1 |
| Co | $Ni^{2+} \rightarrow Ni^{3+}$ | x 2 |
| | $Ni^{2+} \rightarrow Ni^{4+}$ | x 1 |
| Mo | $Ni^{2+} \rightarrow Ni^{3+}$ | x 2 |
| | $Mn^{3+} \rightarrow Mn^{4+}$ | x 1 |
| | $Mo^{5+} \rightarrow Mo^{6+}$ | x 1 |

Synthesis and electrochemical characterization of doped materials

Cobalt-doped LNMO (LNMLO-Co), synthesized by carbonate co-precipitation, was examined to observe the potential predicted decrease in oxygen stability of the cathode material. It is known that Co readily forms a solid solution with LNMLO at large concentrations, allowing an amount of Co to be doped into LNMLO consistent with calculations. The initial charging plateau in the cycling profile is attributed to both reversible anion redox and irreversible oxygen evolution. As predicted computationally, the Co-doped sample shows an extended initial charging plateau relative to the undoped material. As shown in Figure 1.5a, the plateau length of LNMLO is 228.0 mAh/g, while that of LNMLO-Co increases to 266.9 mAh/g. Cycling instability of the material is further presented in the form of the severe voltage decay after 50 cycles, shown in Figure 1.5c. The average voltage retention after 50 cycles decreases from 97% to 93.6% after Co doping. As compared in Figure 1.5e, LNMLO-Co delivers significantly improved discharge capacities in the initial several cycles but drops sharply. The LNMLO-Co shows a first discharge capacity of 290 mAh/g, while that of pristine LNMLO only delivers 220 mAh/g reversible capacity. After 50 cycles, the capacity of LNMLO-Co only maintains 79.3% of initial capacity, 230 mAh/g. Yet, the capacity of LNMLO slightly increases to 232 mAh/g. The experimental observations are in complete agreement with the computational prediction that Co doping leads to decreased oxygen stability, resulting in increased irreversible oxygen gas evolution.

Aiming to provide insight for practical application, obtaining high energy density while maintaining excellent cycling stability, Mo doping is performed on LNMLO-Co material. 1% of Mo was doped into bulk of LNMLO-Co, as will be evident. Consistent with previous literature, 1% is likely near the maximum amount of doping into the structure, due to the large ionic radius of Mo[22]. The first charging curve of LNMLO-CoMo (Figure 1.5b) shows a reduced initial charging plateau (253.4 mAh/g) compared reduction in electron charge transfer from oxygen, which would otherwise accompany the irreversible oxygen loss from the lattice.

**Table 1.3:** A comparison of electrochemical performance parameters of LNMLO, LNMLO-Co and LNMLO-CoMo.



DISTRIBUTION A: Distribution approved for public release

| | Plateau length (mAh/g) | Average voltage (50th Cyc.) | Specific capacity (1st/50th Cyc., mAh/g) | Capacity retention (50th Cyc.) |
|---|---|---|---|---|
| LNMLO | 228.0 | 97.0% | 220/232 | 105% |
| LNMLO-Co | 266.9 | 93.6% | 290/230 | 79.30% |
| LNMLO-CoMo | 253.4 | 94.2% | 297/256 | 86.50% |

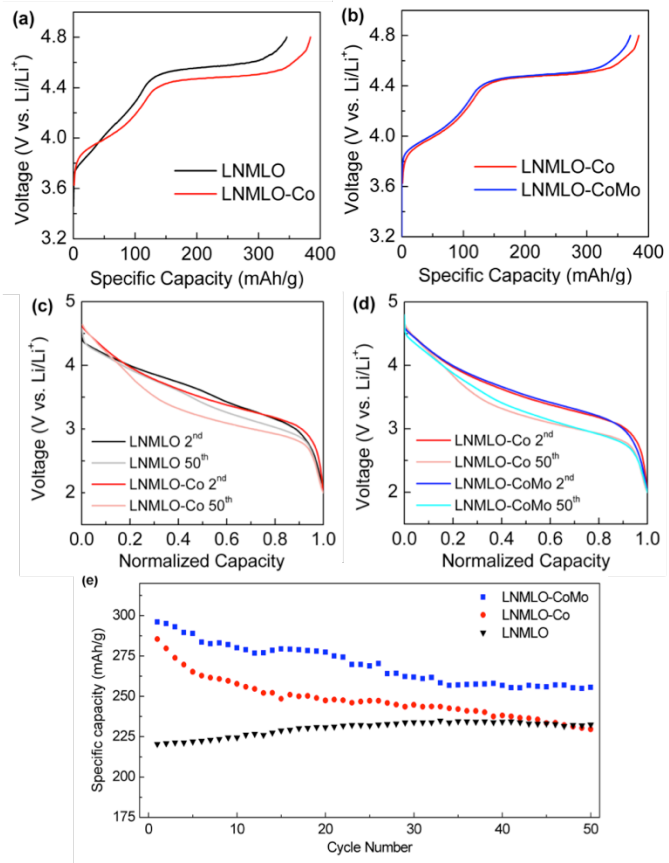


**Figure 1.5:** Cycling results of LNMLO, LNMLO-Co, and LNMLO-CoMo. Incorporation of Co (a) is shown to increase the initial charging plateau, where Mo-doping (b) reduces the plateau, suggesting reduced oxygen gas evolution. Mo-doping further shows reduced voltage decay (d) and improved capacity retention (e).

The material also shows moderately less voltage decay after 50 cycles (Figure 1.5d). The average voltage retention improves by 0.6% with Mo doping. Last, and most notably, the specific capacity and cycling stability are greatly improved. As shown in Figure 1.5e, LNMLO-CoMo delivers a high reversible capacity of 297 mAh/g. After 50 cycles, the capacity remains 256 mAh/g with retention of 86.5%. Note that the columbic efficiency can be further improved if surface treatment could be applied[23] and in this work we focus on the bulk doping only. A detailed electrochemical performances comparison of the three samples is shown in Table 1.3. The results clearly show the positive effect of Mo doping on electrochemical performance.

Electrochemical impedance spectroscopy (EIS) measurements was conducted on the Mo-doped material to investigate the influence of Mo doping on electrochemical behavior, including electronic conductivity and bulk ion diffusion. Before cycling, both LNMLO-Co and LNMLO-CoMo cells show relatively larger charge transfer impedance than that of after cycling, as a formation cycle is needed to reduce the overall resistance. At OCV state, both cells only show one semicircle, which represents charge transfer resistance (RCT). After 30 cycles, an SEI is formed on the surface of cathode materials, and an additional semicircle can be measured at high frequency region, representing resistance of SEI film (RSEI). W is the Warburg impedance related to bulk lithium ion diffusion. The fitting values are



DISTRIBUTION A: Distribution approved for public release

listed in Table 1.4. Mo-doped sample shows reduced RCT before and after cycling, and much smaller RSEI after 30 cycles. It is clearly shows in Figure 6 that after Mo doping, the material exhibits much reduced impedance and improved ionic diffusion. Table 4 lists the quantitatively fitting results of both materials before and after cycling.

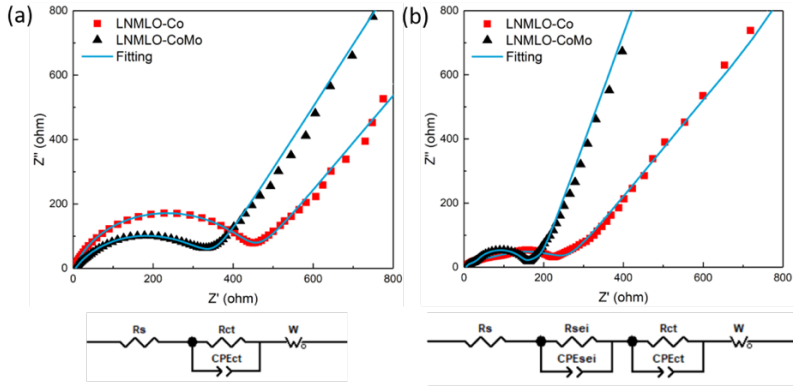


**Figure 1.6:** Nyquist plots of LNMLO-Co and LNMLO-CoMo (a) at OCV and (b) after 30 cycle, with corresponding fitting circuits (below).

**Table 1.4:** EIS fitting results of LNMLO-Co and LNMLO-CoMo at OCV and after 30 cycles.

| | LNMLO-Co (0 Cyc.) | LNMLO-CoMo (0 Cyc.) | LNMLO-Co ($30^{th}$ Cyc.) | LNMLO-CoMo ($30^{th}$ Cyc.) |
|---|---|---|---|---|
| $R_S$ (Ω) | 3.662 | 5.787 | 4.584 | 4.965 |
| $R_{SEI}$ (Ω) | – | – | 44.52 | 24.72 |
| $R_{CT}$(Ω) | 436.4 | 339.5 | 210.3 | 111 |

To confirm the predicted minimal effect on oxygen evolution under alternate doping conditions, Al-doped $Li[Li_{0.2}Ni_{0.19}Mn_{0.59}Al_{0.02}]O_2$ (LNMLO-Al) and Ti-doped $Li[Li_{0.2}Ni_{0.2}Mn_{0.59}Ti_{0.01}]O_2$ (LNMLO-Ti) Li-rich cathode materials were prepared through a hydroxide co-precipitation method. In Figure 1.7(a) and (b), first charging curves of LNMLO-Al and LNMLO-Ti materials both show an oxygen plateau of a similar width to that of the undoped LNMLO. Specifically, the plateau length of LNMLO-Al and LNMLO-Ti are 212 and 206 mAh/g, respectively, near that of pristine LNMLO of 204 mAh/g, indicating Al and Ti doping have a weak influence on oxygen activities; this is in line with calculations, having shown little change in the lowest $E^F_{Ov}$ site. Figure 1.7(c) and (d) show further evidence for the relatively small impact of Al and Ti doping, exhibiting similar voltage decay to the undoped material after 100 cycles. The average voltage retention of LNMLO-Al, LNMLO-Ti and LNMLO are 96.7%, 96.2% and 96.4%, respectively, indicating little change after Al and Ti doping.



DISTRIBUTION A: Distribution approved for public release

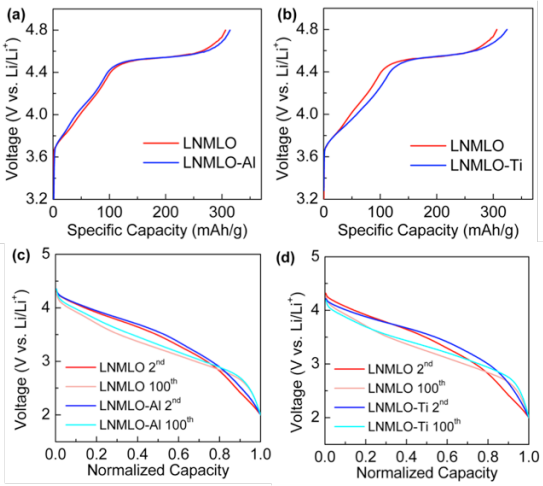


**Figure 1.7:** (a) First charging profiles of LNMLO-Al and LNMLO-Ti materials, compared with pristine LNMLO. Oxygen plateau length of doped materials is similar to that of pristine material, commensurate with DFT calculations. (b) LNMLO-Al, LNMLO-Ti and LNMLO show similar voltage decay after 100 cycles, indicating Al- and Ti- doping does not have influence on electrochemical performance.

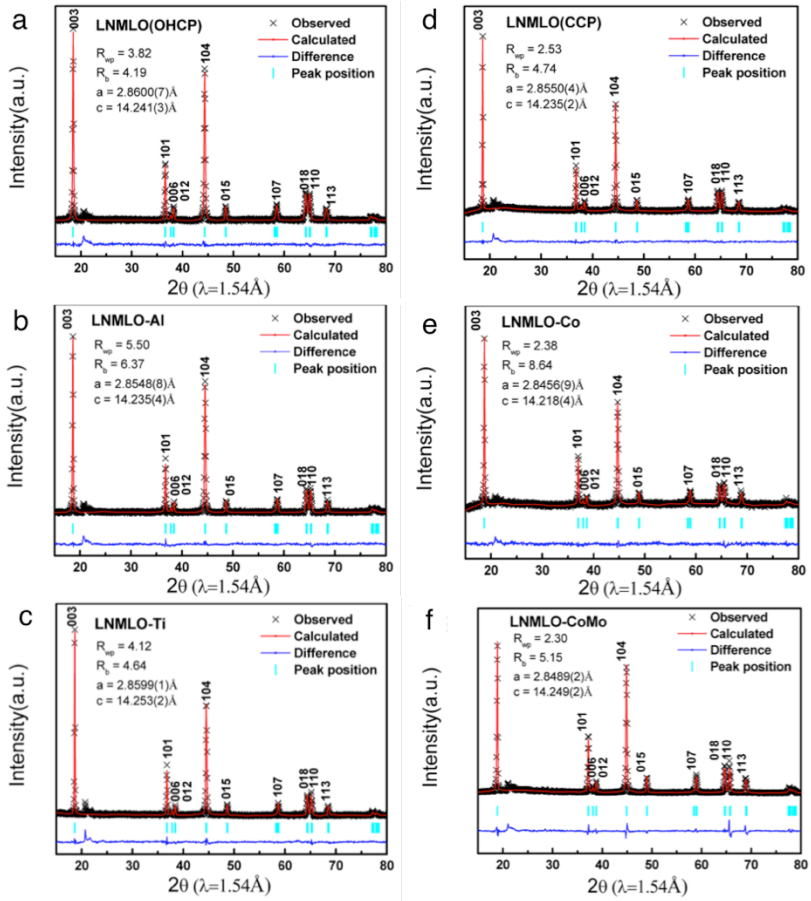


**Figure 1.8:** XRD spectra and Rietveld refinement of pristine $Li_{1.2}Ni_{0.2}Mn_{0.6}O_2$ (a) and Mo-doped material (b).

(Table 1.5). It was predicted that Al-doping results in a slight contraction of the a- and c-lattice parameters, showing reduced bond lengths in the $MO_6$ octahedron. Further consistent with experiment, Ti is predicted to expand the c lattice parameter, due to the increased Ti-O bond lengths relative to the



DISTRIBUTION A: Distribution approved for public release

replaced Mn-O bond lengths. As shown in Figure 1.7 and Table 1.5, experimental fittings show these values to generally follow the predicted trends. The XRD results suggest Al and Ti have been successfully doped into the structure.

**Table 1.5:** Lattice parameters from DFT calculation (Theoretical) and from Rietveld refinement (Experimental) for Al and Ti doping.

| | Theoretical | | Experimental | |
|---|---|---|---|---|
| | a=b (Å) | c (Å) | a=b (Å) | c (Å) |
| Undoped | 2.908 | 14.435 | 2.8600(7) | 14.241(3) |
| Al | 2.897 | 14.421 | 2.8548(8) | 14.235(4) |
| Ti | 2.907 | 14.482 | 2.8599(1) | 14.253(2) |

The incorporation of Co and Mo into the structure was verified by X-ray diffraction (XRD), X-ray photoemission spectroscopy (XPS), and energy dispersive X-ray spectroscopy (EDS) of focused ion beam cross-sectioned secondary particles (FIB-EDS). Figure 1.7d-f compares XRD and Rietveld refinement results of LNMLO, LNMLO-Co and LNMLO-CoMo materials. The lattice parameter variation trend of the three materials is shown in Figure 1.9. $Co^{3+}$ (0.545 Å) doping leads to shrinking of a- and c- lattice parameters compared with pristine LNMLO. A slight a-lattice expansion is caused by $Mo^{5+}$ (0.61 Å) substitution into the structure, also noting that $Mo^{5+}$ doping causes significant expansion of c-, due to the increased Mo-O bond length. The increased c-lattice parameter facilitates $Li^{+}$ diffusion, explaining in part the increment of capacity in LNMLO-CoMo material. It is

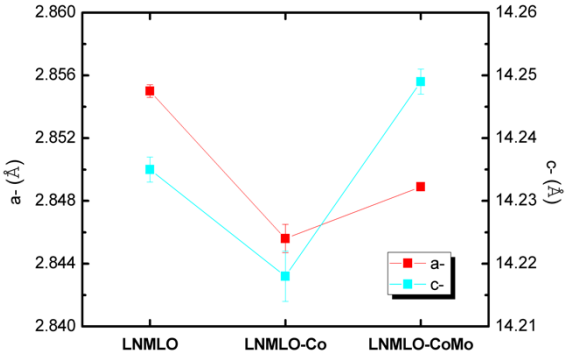


**Figure 1.9:** Lattice parameters of LNMLO, LNMLO-Co and LNMLO-CoMo as determined by Rietveld refinement of XRD spectra (Figure 1.7).

noted that doping of Mo into the LNMLO-Co structure was limited to 1-2% Mo. Figure 1.10 clearly shows the formation of impurity phases upon doping of Mo at a concentration of 3%. Future efforts will be made with alternate synthesis methods, including polyl synthesis, which eliminates the required high temperature processing.

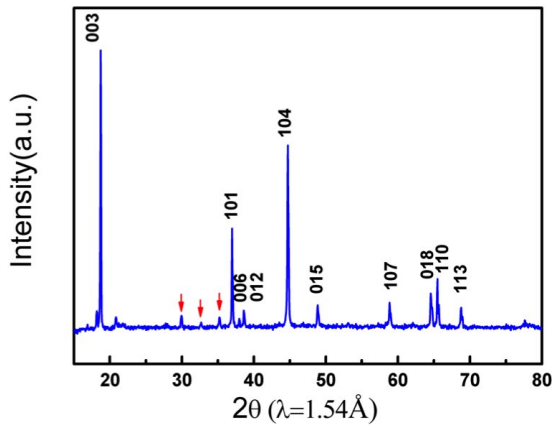




DISTRIBUTION A: Distribution approved for public release

**Figure 1.10:** Mo doping of 3% shows the formation of impurity phases, indicated by red arrows.

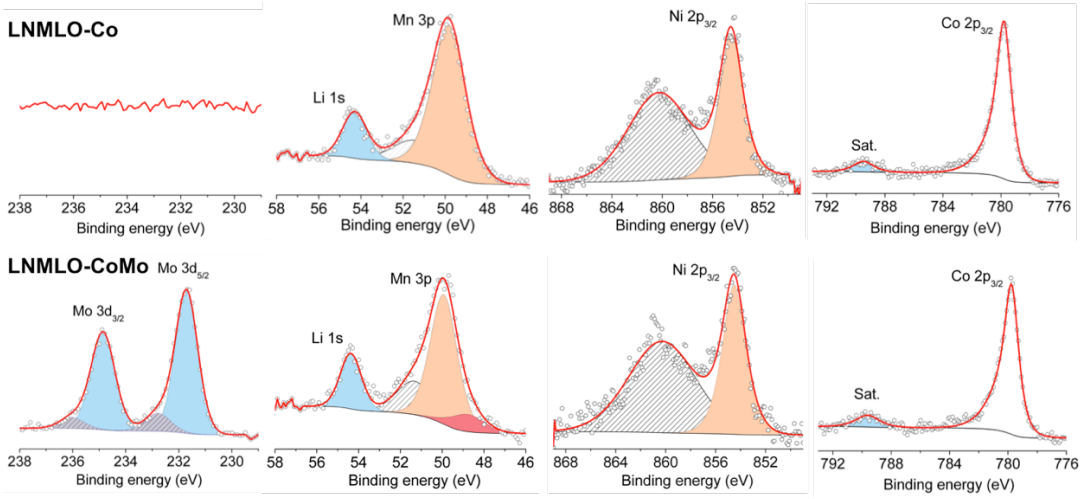


**Figure 1.11:** XPS of LNMLO-Co and LNMLO-CoMo show that Mo took the predicted $Mo^{5+}$ valence. Results further show a portion of the Mn is reduced from $Mn^{4+}$ to $Mn^{3+}$.

Figure 1.11 compares the XPS analysis of LNMLO-Co and LNMLO-CoMo samples. Results of the XPS suggest that most of the Mo dopant takes the $Mo^{5+}$ oxidation state in the pristine state. Specifically, the two peaks at binding energies of 231.7 eV and 234.8 eV are attributed to $Mo^{5+}$. Weak shoulders at higher binding energy of 232.8 eV and 236 eV indicate a small amount of $Mo^{6+}$.[24] This matches the predicted values based on magnetization data (Table 2), and calculate Mo in the pristine state to have a +5 charge. This dopant is predicted to be oxidized to $Mo^{6+}$ on the first delithiation, not explored in this work. Oxidation states of Ni show no change, as the peak at 854.5 eV does not shift after Mo doping. Mn appears to be slightly reduced, again consistent with computation results. The predicted mixed valence of Mn may enhance the conductivity of the material, partially explaining the increased specific capacity.[22] Co is slightly reduced after Mo doping, as the satellite peak area

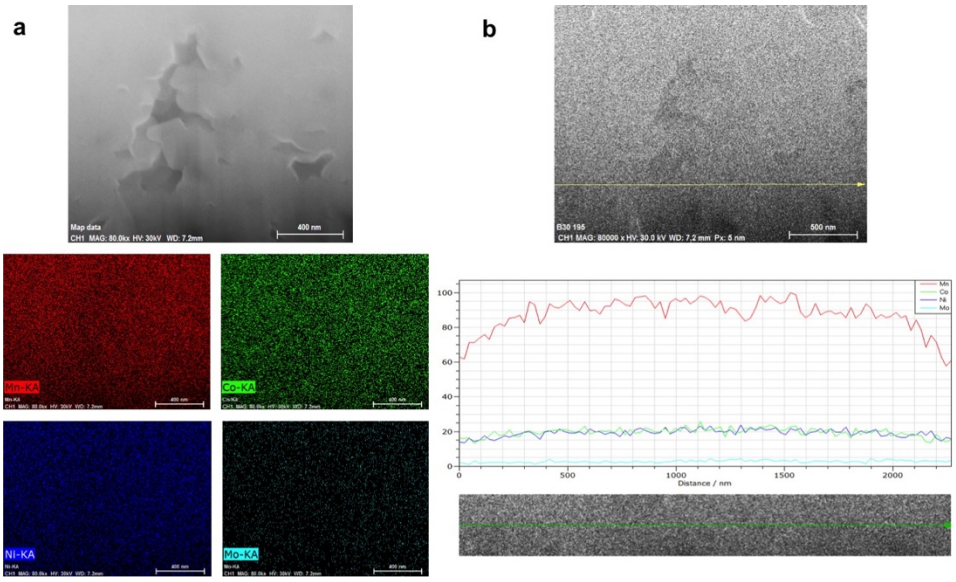


**Figure 1.12:** A FIB cross-sectioned secondary particle of LNMLO-CoMo, showing uniform distribution of elements through the particles, and no signs of accumulation at particle boundaries.



DISTRIBUTION A: Distribution approved for public release

increases from 6.84% to 8.99% after doping. Further evidence of a homogeneous distribution of the Mo dopant was observed by focused ion beam cross-section of a secondary particle coupled with EDS, as shown in Figure 1.12. These preliminary EDS results show an even distribution, though the technique is ultimately limited by its low spatial resolution (~1 um), and further testing is required in scanning transmission electron microscopy (STEM) for verification of the full incorporation of Mo. It is noted that Mo-doping has indeed been explored for lithium rich layered oxides $Li_2MnO_3$,[25] $Li[Li_{0.2}Ni_{0.2}Mn_{0.6}]O_2$,[22] and $Li[Li_{0.2}Mn_{0.54}Ni_{0.13}Co_{0.13}]O_2$,[26,27] and in the case of $Li_2MnO_3$, $Mo^{5+}$ was observed by X-ray absorption spectroscopy. Though again, little to no emphasis was placed on the stabilization of oxygen within the lattice in these prior works.

It is noted, however, that the limited resolution present in SEM-based EDS maps may not enable clear distinction between non-uniformities in dopant distribution, due to the relatively high interaction volume of x-rays within a surface.[28] As such, TEM and STEM were employed, allowing a higher-resolution view of the elemental distribution. The convincing evidence of dopant incorporation comes in the form of aberration corrected high angle annular dark field (HAADF) STEM images of pristine particles (Figure 1.13). Incorporation of Mo is clearly correlated with an increase in lattice strain, as evident by the contrast non-uniformity in the doped particle (Figure 1.13a). Transition metal migration to the lithium layer was observed near the particle sub-surface, likely correlated with the increased strain (Figure 1.13b).[29] HAADF image of the pristine LNMLO-Co shows a typical structure with well layered properties in the bulk of the pristine material extended to the surface (Figure 1.13c). (4) EDS mapping of a primary particle of LNMLO-CoMo acquired in STEM shows a uniform distribution of all transition metal constituents (Figures 1.13e-h). Quantitative data acquired by line scan (Figure 1.13d) show the transition metals in the appropriate concentration from synthesis, and further illustrate the uniform distribution through the surface and bulk (Figure 1.13i).

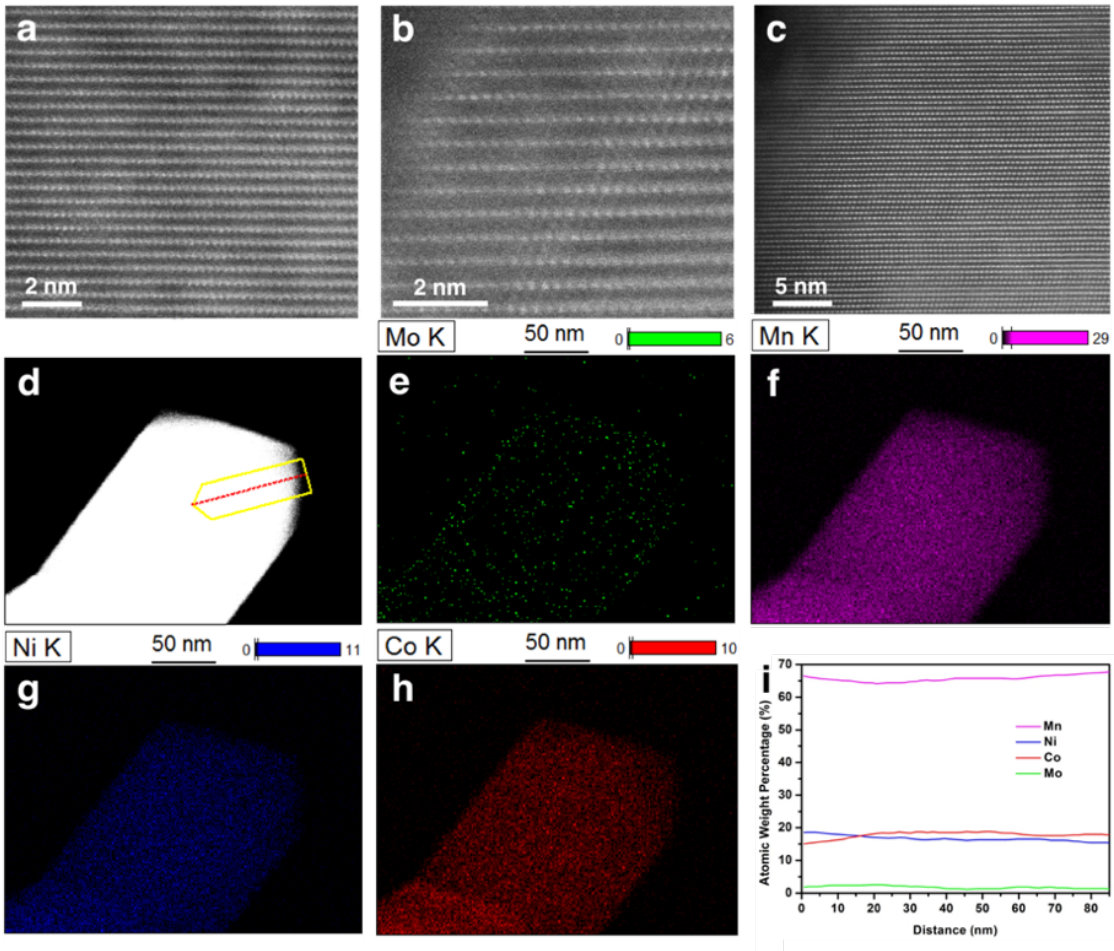




DISTRIBUTION A: Distribution approved for public release

**Figure 1.13:** HAADF images of pristine LRLO-CoMo (a) bulk and (b) surface, and (c) pristine LRLO-Co, showing both surface and bulk. STEM/EDS mapping of a primary particle show a uniform distribution of all constituents (e-h). Quantitative analysis (i) was attained by an EDS line-scan, acquired along the red line in the direction of the yellow arrow in (d).

## 2. Surface coatings for improved capacity retention

### Background and goals

The enhanced oxygen activity, which make LRLO desirable in the first place, also make surfaces especially susceptible to oxygen evolution and subsequent phase change. Previously d emonstrated through joint computational and STEM-EELS study, oxygen becomes unstable at high state of charge, ultimately resulting in oxygen vacancy formation.[5] This is especially pre valent at surfaces, where undercoordinated oxygen is present. These oxygen vacancies result in the formation of defect spinel, and such surface phase transformations are well known to be s ources of capacity loss and reduced rate capability. Lithium lanthanum titanate ($Li_{3x}La_{(2/3)-x}\square_{(1/3)-2x}TiO_3$, LLTO), a fast lithium ion conducting perovskite solid-electrolyte, has been demonstrate d in the past as a successful coating material when applied to $Li(Ni_{0.8}Co_{0.15}Al_{0.05})O_2$ (NCA), s howing notably improved electrochemical performance.[30] Previous attempts to prevent surface oxygen loss and surface modification in LRLO materials have also been demonstrated using a number of methods, including surface modification through the chemical induction of oxygen vacancies,[23] surface modification through heat treatment,[31] and application of surface coatings.[32] Stable oxide coatings such as LLTO offer the potential to reduce the concentration gradient of oxygen diffusion at the surface of LRLO at high voltage, and reducing such surface phase tra nsformations from occurring. Coupled with LLTO's high ionic conductivity, LLTO is tested as a coating material to determine potential improvement in particle cyclability.

Experimental Methodology and Results

Secondary particles of LRLO $Li_{1.13}Ni_{0.3}Mn_{0.567}O_2$ (LNMO) were synthesized via carbonate coprecipitation, as described in a previous section. In order to incorporate LLTO as a surface coatings, LLTO precursors were mixed and calcined with varying weight percentages and calcination temperatures. XRD clearly shows the lack of a crystalline peak for LLTO (at 32.3°) below 800 °C, suggesting 800 °C is required to crystallize the surface coating. To determine uniformity and morphology of the surface coatings, SEM was performed, suggesting no morphological changes of the LNMO at both 1 wt% LLTO and 2 wt% LLTO with calcination temperatures of 800 °C.



DISTRIBUTION A: Distribution approved for public release

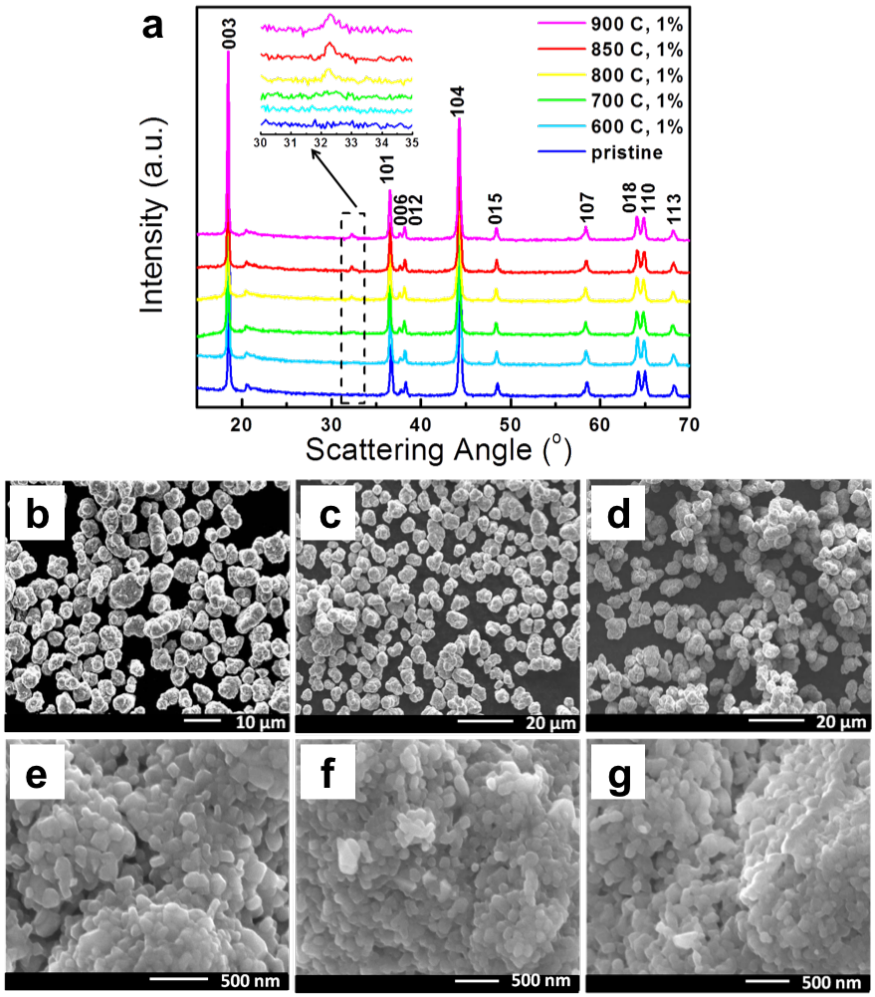


**Figure 2.1:** XRD of 1 wt% LLTO incorporation for a range of calcination temperatures from 600 °C to 900 °C. SEM images: (a and b) LNMO; (c and d) 800 °C, 1 wt% LLTO coated LNMO; (e and f) 800 °C, 2 wt% LLTO coated LNMO.

Having demonstrated the presence of a uniform coating via SEM, and verifying appropriate crystallinity by XRD, coated powders were cycled to observe the correlation between weight percent, crystallinity, and cyclability. Cycling was performed for most calcination temperatures with 1 wt% LLTO coating, and tested for varied weight percent coatings at a constant calcination temperature of 800 °C. Cycling data is presented in Figure 2.2. Results of cycling show a few clear trends. Increased calcination temperature shows a general improvement during charge at a rate of C/20. However, the coulombic efficiency and discharge capacity both drop notably at calcination at 900 °C. Similarly, the discharge capacity at 1C shows decreased specific capacity when calcined above 800 °C. As such, results generally point to 1 wt% calcined at 800 °C as optimal conditions for improved cyclability. Furthermore, such conditions show the most notable improvement in capacity retention.



DISTRIBUTION A: Distribution approved for public release

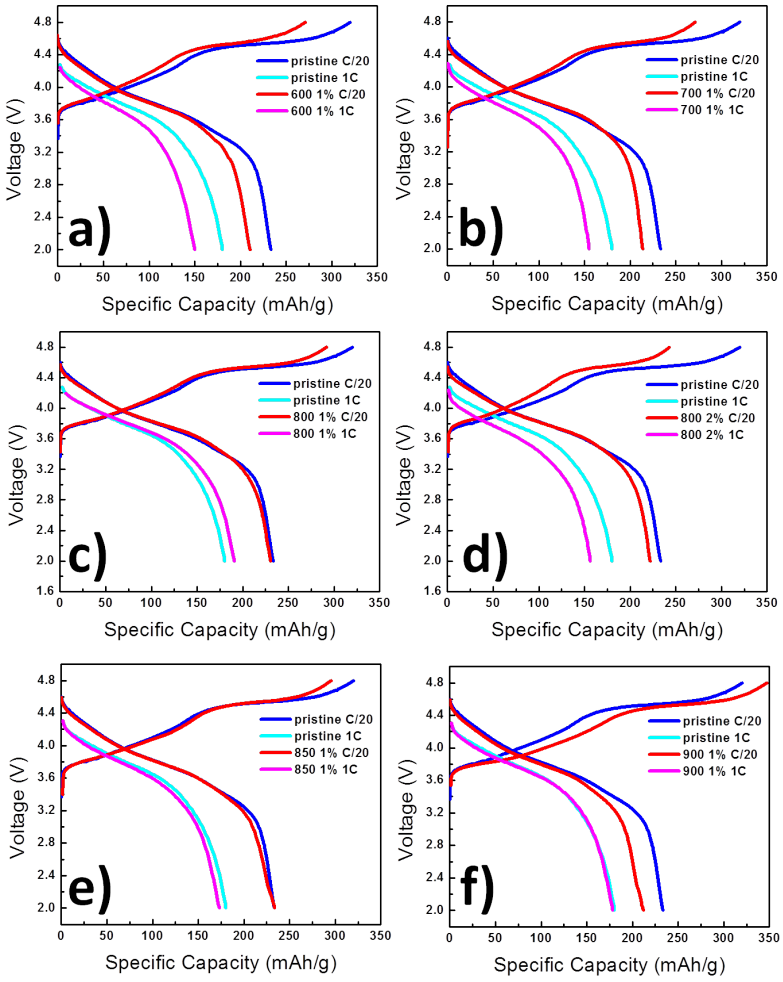


**Figure 2.2:** Comparison of first cycle charge/discharge voltage profile and high rate discharge voltage profile between LNMO and LLTO coated LNMO: (a) 600 °C, 1% LLTO coating, (b) 700 °C, 1% LLTO coating, (c) 800 °C, 1% LLTO coating, (d) 800 °C, 2% LLTO coating, (e) 850 °C, 1% LLTO coating, and (f) 900 °C, 1% LLTO coating. The voltage range is 2.0−4.8 V at 1 C = 250 mA $g^{-1}$.

With 1 wt% LLTO-coated LRLO calcined at 800 °C having the most desirable performance, this material was further investigated via STEM-EELS. To further verify the uniformity of the LLTO coating, bright field STEM coupled with EELS were applied to the uncoated and coated LLTO Li-rich material. Figure 2.3a and b compares the STEM images of the uncoated and coated Li-rich material. The uncoated particles have a clean surface with Li and TM layers extending to the outermost surface. After LLTO coating, there is a uniform nanoscale layer (less than 1 nm in thickness) found on the particle surface. The EELS experiments were carried out on both bulk and surface region of LLTO coated Li-rich (Figure 2.3c). The data points are aligned with the BF image (Figure 1b) to indicate where each spectrum was taken (shown in red and black). There is a clear Ti-L edge peak in the spectra obtained on the surface region, where Ti-L3 and Ti-L2 were induced by the electron transitions from $2p^{3/2}$ and $2p^{1/2}$, respectively, to unoccupied 3d orbitals. This Ti-L edge disappears in the bulk region of the material,



DISTRIBUTION A: Distribution approved for public release

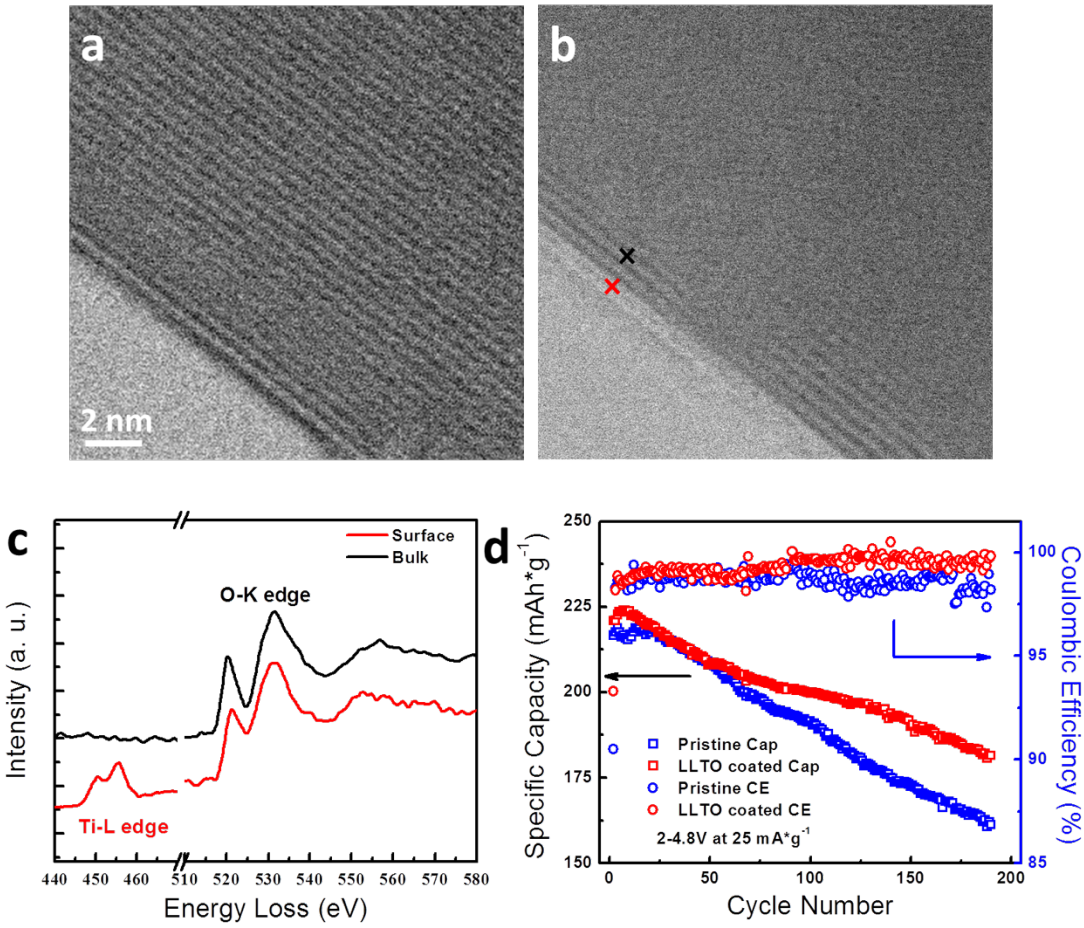


**Figure 2.3:** STEM/ABF images of (a) uncoated Li-rich material and (b) 1 wt% LLTO coated Li-rich. (c) EELS spectra of 1 wt% LLTO coated Li-rich at different regions. (d) Comparison of capacity and coulombic efficiency for uncoated and LLTO coated Li-rich over the course of 190 cycles.

which indicates LLTO is only the surface. It should be noted that the La-M edge was not detected since it overlaps with Ni-L edge. Both materials were cycled at a slow rate of 25 mA $g^{-1}$ (C/10) between 2-4.8 V. The uncoated Li-rich material shows only 74.2% capacity retention after 190 cycles, while the LLTO coating improves the capacity retention to 82.3%. In addition, the LLTO coated Li-rich delivers higher coulombic efficiency than the uncoated upon the long term cycling. The results indicate that nanoscale uniform crystalline LLTO surface coating could improve the cycling stability significantly.

## 3. Impact of nanostructuring on electrochemical performance and rate capability

### Background and goals

As previously described, surface structure modification plays an important role in the degradation of cyclability in LRLO. Intuitively, the volume fraction of surface defect-spinel present in a particle increases with decreasing particle size. More specifically, Dahn et al.[33] reported that layered and spinel phase separation appears in LRLO samples with large particles while small particle samples are small enough that they are entirely composed of the surface spinel phase present in the large particle samples. This phenomenon indicates the importance of mesoscale material modification, and that material variations on the secondary particle level will have an effect on electrochemical performance. Control of the arrangement of primary particles during synthesis can be correlated to the porosity and density of the secondary particles. Further, variations in in mechanical properties of secondary particles can also influence the strain evolution during cycling. Based on these hypotheses, efforts



DISTRIBUTION A: Distribution approved for public release

were put to study the difference in the mesostructure of secondary particle as well as how these differences could affect the electrochemistry performance of LRLO materials.

To observe the impact of mesostructured modification, $Li[Li_{0.2}Ni_{0.2}Mn_{0.6}]O_2$ (LNM13) with varied secondary particle size and surface roughness were studied. It is demonstrated that particle stirring time has a notable effect on the mesostructured of secondary particles. The crystal structure and chemical composition of synthesized samples were confirmed to be same through XRD Rietveld refinement and inductively coupled plasma atomic emission spectroscopy (ICP-AES). Materials with varied mesostructured were inspected for morphological difference to correlate with electrochemistry performance.

**Experimental Methodology**

LNM13 materials are synthesized through pH-controlled co-precipitation method. An aqueous solution containing $Ni(NO_3)_2 \cdot 6H_2O$, $Co(NO_3)_2 \cdot 7H_2O$ and $Mn(NO_3)_2 \cdot 4H_2O$ is reacted with a $Na_2CO_3$ solution under a controlled pH of 7.8 to 7.85 during the entirety of the process. Different concentrations of $TM(NO_3)_2$ solution and $Na_2CO_3$ solution were used to study the factors supporting formation of big particles. Ammonia was also used in some of the controlled experiments to study the effect of chelating agent in supporting the formation of larger particles. In all the experiments, stirring speed was consistently 500 rpm at the beginning and gradually increased to 750 rpm over the course of the synthesis. $Ni_{1/4}Mn_{3/4}CO_3$ (NM13-precursor) obtained from the reaction described above was aged at 80 °C for 12 hours. Then the NM13-precursor was washed 4 times by DI water and dried in vacuum oven at 80 °C overnight. After that, the NM13-precursor was mixed with a stoichiometric amount of $Li_2CO_3$ and sintered at 500 °C for 5 hours, then heated up to 800 °C for 15 hours. Heating speed was 5 °C/min. After the calcination, the product LNM13 was cooling to room temperature in the oven.

The as-synthesized LRLO active material was mixed with polyvinylidene fluoride (PVDF) and acetylene black (Super C65) to prepare the cathode. The mass ratio of active material: PVDF: Super C65 is 8:1:1. The mix is then well dissolved in a proper amount of N-Methyl-2-pyrrolidone (NMP) with magnetic stirring at 700 rpm for 20 hours. After magnetic stirring, the slurry was casted onto Al foil and dried at 80 °C in vacuum oven for 12 hours. The loading mass of each Al foil is 7.22 mg. CR2016 coin cells are assembled in the glove box under argon atmosphere, with lithium metal as anode and 1M LiPF6 in EC:DMC = 3:7 (V:V) as electrolyte.

**Table 3.1:** Synthesis conditions used for secondary particle preparation and respective average particle size.

| Exp. | C(acid) | C(base) | NH3 | Temp. (°C) | Aging/Stirring | Avg. dP (µm) |
|---|---|---|---|---|---|---|
| 1 | 1M | 0.2M | - | RT | Aging | 3 |
| 2 | 1M | 0.2M | 0.03M | RT | Aging | 3 |
| 3 | 1M | 1M | 0.15M | RT | Aging | 3.1 |
| 4 | 1M | 1M | - | 80 | Aging | 3.8 |
| 5 | 1M | 1M | 0.15M | 80 | Aging | 4.1 |
| 6 | 1M | 1M | 0.15M | 80 | Stirring | 6.4 |

**Results and Discussion:**

A series of controlled experiments were designed to explore the formation of large NM13-precursor particles by carbonate co-precipitation synthesis. Different synthesis conditions and resulting average particle size are listed in Table 3.1, in which $TM(NO_3)_2$ solution concentration (denoted as C(acid)), $Na_2CO_3$ solution concentration (denoted as C(base)), addition of ammonia, temperature of reaction, and the choice of stirring or aging after reaction are studied. The average particle size of each NM13-precursor sample shows high concentrations of neither $TM(NO_3)_2$ solution or $Na_2CO_3$ solution cause significant change in the particle size; high reaction temperature, addition of ammonia and maintained stirring of the solution after reaction all support the formation of larger



DISTRIBUTION A: Distribution approved for public release

secondary particles. Clearly, the most notable change was acquired with enhanced stirring, following the aging process (Exp. 6). This produced secondary particles over twice as large in diameter as those

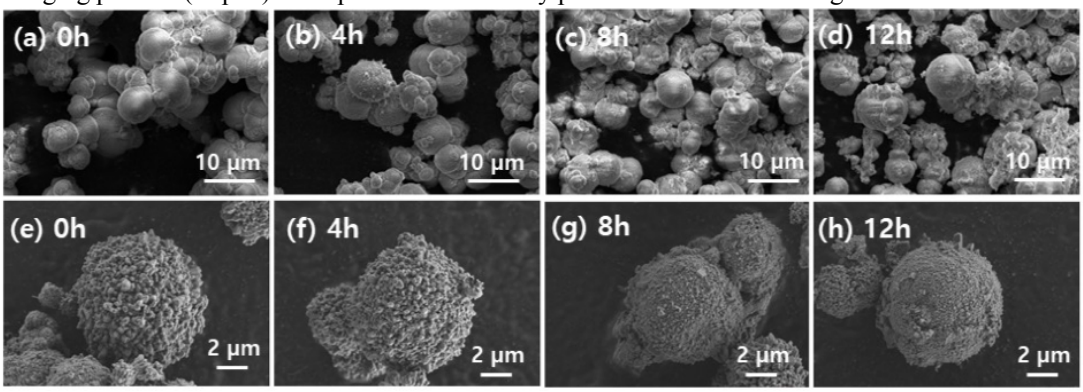


**Figure 3.1:** (a)-(d) NM13-precorsors with varied stirring times after reaction. (e)-(h) Precursors for the same stirring times after calcination.

without stirring. To verify the particles are fundamentally similar, XRD and electrochemical testing was performed. XRD refinement shows both samples exhibit proper crystallinity and electrochemical testing shows similar behavior during the 1st charge/discharge curve of both samples, delivering specific discharge capacity of 182-184 mAh/g. This drastic particle size change drove the stirring process as the main focus of the following experiments.

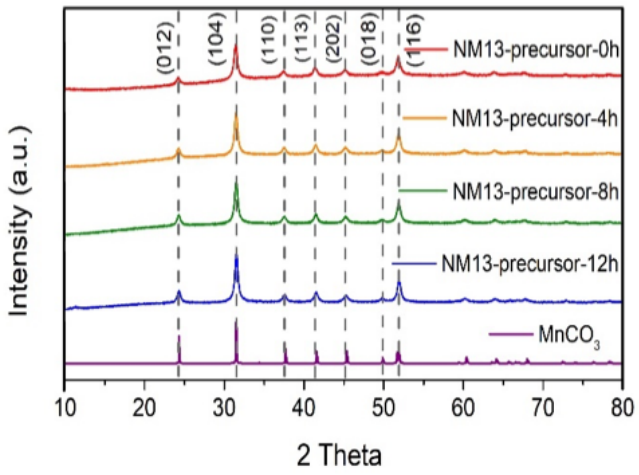


**Figure 3.2:** XRD patterns as a function of stir time.

LNM13 samples with different surface roughnesses were then synthesized with the same co-precipitation parameters of Exp. 6 in Table 3.1, having produced the larger secondary particles. Varied stirring times after the reaction were then applied to obtain varying surface roughness. Figure 3.1(a)-(d) shows the morphology of NM13-precursors with (a) 0 h, (b) 4 h, (c) 8 h, and (d) 12 h stirring time. All the precursors are spherical particles with an average particle size around 6μm. Figure 3.1(e)-(h) are SEM images of LNM13 active materials calcinated from precursors with different stirring time. Those LNM13 samples are denoted as LNM13-0h, LNM13-4h, LNM13-8h, and LNM13-12h based on the stirring time of their precursors. SEM images show that with increased precursor stirring time, the LNM13 materials have a smoother surface. XRD patterns of different NM13-precurosrs and LNM13 active materials are compared in Figure 3.2. All the precursors can be indexed to R-3c space group while all the NM13 active materials belong to R-3m space group, which indicates the synthesized precursors and active materials are all pure phase materials and are consistent with previously produced samples. The composition of the NM13-precursors was qualitatively confirmed by ICP as well, indicate that all the samples have Mn/Ni ratio within normal deviation range, which indicates these samples have same chemical composition as designed.



DISTRIBUTION A: Distribution approved for public release

Using high resolution SEM, it is further shown that LNM13-0h, which has a relatively rough surface, consist of primary particles with a size around 300 nm; conversely, LNM13-12h consist of primary particles with particle size around 100 nm. The roughness of secondary particle surface

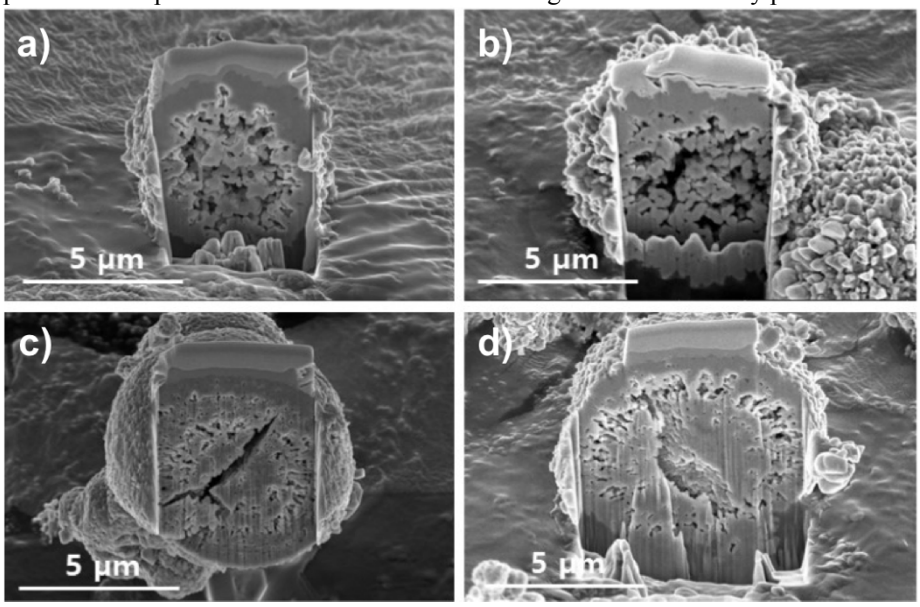


**Figure 3.3:** Cross-sectional views of secondary particles not stirred (a,b) and stirred for 12 hours (c,d) showing modified particle density. Notable cracking is observed for the sample stirred for 12 hours.

reflects the size of their primary particles. It is still unclear why different stirring time can yield final products with such different morphology. Both sample have same pore size peak at 4.5 nm. However, LNM13-0h has a specific surface area of 3.16$m^2$/g while LNM13-12h only has a specific surface area of 2.67 $m^2$/g based on BET test results. This indicates that LNM13-0h is more porous than LNM13-12h.

Cross-sectional FIB images of LNM13-0h and LNM13-12h are shown in Figure 3.3. FIB was used to cut the spherical particles. Figure 3.3(a) and 3.3(b) are from LNM13-0h, which shows a porous and loose structure around the center of secondary particles. A large amount of porosity can be clearly seen in the bulk of LNM13-0h. Figure 3.3(c) and 3.3(d) are cross-section images of LNM13-12h which has a denser bulk morphology. In the center of some secondary particles of LNM13-12h, sharp cracking can also be observed. The cross-section images of these two samples confirmed that LNM13-0h has higher porosity than LNM13-12h.

The first charge/discharge curve of LNM13 samples with different surface roughness is shown in Figure 3.4(a). LNM13-0h, LNM13-4h, LNM13-8h, and LNM13-12h delivers a first cycle discharge capacity of 137 mAh/g, 154 mAh/g, 158 mAh/g and 182 mAh/g, respectively. The rate for the first cycle is C/20 (12.5 mA/g) for all the samples. The different first cycle behavior may come from different electronic conductive network of two sample. Despite the difference in first cycle discharge capacities, the charge curves of all samples show similar behavior. The sloping region around 4.2 V and the oxygen plateau above 4.5 V can be clearly seen in all the samples.

The cycling performances of four samples are illustrated in Figure 3.4(b). Except the first cycle, rest cycles are tested under C/10 (25 mA/g). All the samples experienced increase of their discharge



DISTRIBUTION A: Distribution approved for public release

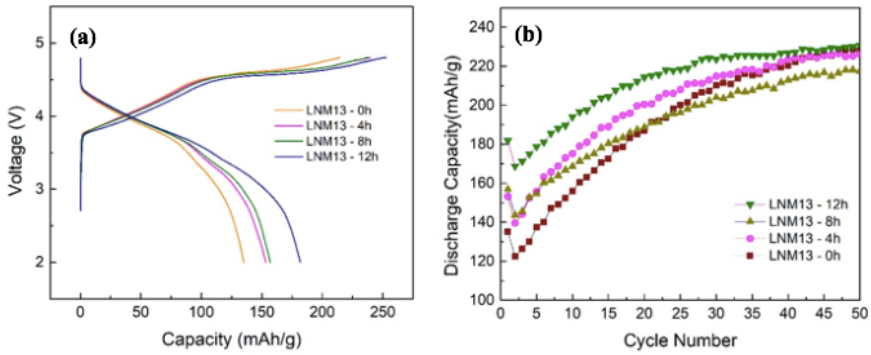


**Figure 3.4:** (a) First cycle charge/discharge profile and (b) cycling performance of LNM13 as a function of stirring time.

capacity over rest cycles, which is consistent with the performance of typical pH-and-morphology-controlled LNM13. After 50 cycles, LNM-0h, LNM-4h, LNM-8h, and LNM-12h delivers a discharge capacity of 220 mAh/g, 218 mAh/g, 211 mAh/g, and 222 mAh/g, respectively. LNM-0h experienced an increase in capacity of 59.4% compared to first cycle; while LNM-12h experienced an increase of 21.9% compared to its first cycle. The large increase in discharge capacity indicates that LNM13-0h has similar capacity as LNM13-12h after cycles, but a large portion of its capacity cannot be fully discharged when it starts to charge and discharge at the beginning.

**Summary and outlook**

Great progress was made to determine causes of structural instability and to mitigate such instabilities in LRLO. Doping of a model layered Li-rich nickel manganese material was investigated via DFT calculations to explore stabilization of oxygen ions in the material, and guided by results, experimental doping and characterization was performed. The theoretical model was validated, as compared to previously published work on the evolution of oxygen vacancies. Of all dopants simulated, Mo and Ru were shown to increase the oxygen vacancy formation energy, $E_{Ov}^{F}$, elucidating the potential to reduce oxygen evolution during cycling and improving overall capacity retention. This improved $E_{Ov}^{F}$ was attributed to a delocalization of the Mo electrons to the surrounding anions, serving to stabilize the oxygen ions by creating a larger barrier for charge transfer. Beyond pure understanding of the effect of dopants on the $E_{Ov}^{F}$ this work uncovered fundamental characteristics of degradation mechanisms within this class of materials. Closer inspection of the local environments surrounding anions in these materials uncovered trends in stability and bonding.

A variety of dopants were introduced to Li-rich material through co-precipitation synthesis methods. As predicted by the computation results, both Al and Ti doping have no impact on the formation of oxygen vacancies as observed by the high-voltage plateau width. Conversely, Co-/Mo-doping increases/decreases the width of the plateau, respectively, and incorporation of Mo is shown to improve capacity retention. To confirm the total incorporation of the Mo dopant into the bulk of the material, STEM/EDS will be performed, eliminating the potential for particle boundary accumulation effects.

LLTO coating was applied to LRLO, showing notable improvement in cyclability. Specific coating amounts and calcination temperatures were explored. Having determined that both 1 wt% and 2 wt% both crystallize on the cathode particles without altering morphology, 1 wt% LLTO coated material was explored for calcination studies. XRD showed that heating to 800 °C was required for good crystallinity, while electrochemical cycling showed calcination above 800 °C reduced cyclability.

To explore mesoscale modification, LNM13 samples with different particle size and surface roughness were synthesized through pH-controlled co-precipitation. Particle size modified to be between 3 µm and 6 µm by careful control of processing conditions. Addition of ammonia, high reaction temperature, and stirring the solution after reaction are three main factors that support the formation of large particles. XRD and ICP results verified similar crystal structure and chemical composition. The full range of particles did not showed no significant difference in their first cycle capacity, but after 50 cycles, the larger particles showed higher capacity (230 mAh/g) than the smaller particles (222 mAh/g).



DISTRIBUTION A: Distribution approved for public release

Different stirring time after the co-precipitation reaction can yield LNM13 samples with different surface roughness, which was later explained by high resolution SEM that the difference of roughness can be described as primary particle size. LNM13-12h has relatively smooth surface and smaller primary particles (~100 nm) while LNM13-0h has relatively rough surface and larger primary particles (~300 nm). BET results show that LNM13-12h has lower specific surface area than LNM13-0h when they both have same pore size distribution, which indicates LNM13-12h is less porous than LNM13-0h. Cross-section images of both samples were taken through FIB. LNM13-12h shows relatively dense bulk morphology or sharp cracking; while LNM13-0h has a large amount of cavities around the center. LNM13 samples with different surface roughness show different first capacity in the electrochemistry test. It is clearly shown in the voltage profile that LNM13-0h has much lower first cycle discharge capacity (137 mAh/g) than LNM13-12h (182 mAh/g). After 50 cycles, however, LNM13-0h and LNM13-12h exhibits similar discharge capacity of 220 mAh/g and 222 mAh/g, respectively.

Such results demonstrate both the importance of predictive modeling and careful control of processing parameters. By controlling the ability of oxygen to move through the structure, the original structure may be preserved within bulk and at the surfaces, promoting reduced voltage fade, improved capacity retention, and improved rate capability. While further control of defects will be required for commercial application of LRLO materials, these results point to control of defects—oxygen vacancies in particular—as a key to enabling LRLO as a material for high energy density cathode materials in the next generation of lithium ion batteries.

**References**


1. Goodenough, J. B. & Park, K.-S. S. The Li-ion rechargeable battery: A perspective. *J. Am. Chem. Soc.* **135,** 1167–76 (2013).
2. Yu, H. & Zhou, H. High-Energy Cathode Materials ($Li_2MnO_3$-$LiMO_2$) for Lithium-Ion Batteries. *J Phys Chem Lett* **4,** 1268–1280 (2013).
3. Xu, B., Fell, C. R., Chi, M. & Meng, Y. S. Identifying surface structural changes in layered Li-excess nickel manganese oxides in high voltage lithium ion batteries: A joint experimental and theoretical study. *Energy Environ. Sci.* **4,** 2223–2233 (2011).
4. Singer, A. *et al.* Nucleation of dislocations and their dynamics in layered oxide cathode materials during battery charging. *Nat. Energy* (2018). doi:10.1038/s41560-018-0184-2
5. Qian, D., Xu, B., Chi, M. & Meng, Y. S. Uncovering the roles of oxygen vacancies in cation migration in lithium excess layered oxides. *Phys. Chem. Chem. Phys.* **16,** 14665–14668 (2014).
6. Chu, I. H. *et al.* Room-Temperature All-solid-state Rechargeable Sodium-ion Batteries with a Cl-doped $Na_3PS_4$ Superionic Conductor. *Sci. Rep.* **6,** (2016).
7. Wu, E. A. *et al.* New Insights into the Interphase between the Na Metal Anode and Sulfide Solid-State Electrolytes: A Joint Experimental and Computational Study. *ACS Appl. Mater. Interfaces* **10,** 10076–10086 (2018).
8. Liechtenstein, A. I., Anisimov, V. I. & Zaanen, J. Density-functional theory and strong interactions: Orbital ordering in Mott-Hubbard insulators. *Phys. Rev. B* **52,** R5467 (1995).
9. Chevrier, V. L., Ong, S. P., Armiento, R., Chan, M. K. Y. & Ceder, G. Hybrid density functional calculations of redox potentials and formation energies of transition metal compounds. *Phys. Rev. B* **82,** 075122 (2010).
10. Lutfalla, S., Shapovalov, V. & Bell, A. T. Calibration of the DFT/GGA+U method for determination of reduction energies for transition and rare earth metal oxides of Ti, V, Mo, and Ce. *J. Chem. Theory Comput.* **7,** 2218–2223 (2011).
11. Hinuma, Y., Meng, Y. S., Kang, K. & Ceder, G. Phase Transitions in the $LiNi_{0.5}Mn_{0.5}O_2$ System with Temperature. *Chem. Mater.* **19,** 1790–1800 (2007).
12. Kamisaka, H., Hitosugi, T. & Yamashita, K. First-principle calculations of dopant-oxygen vacancy complexes in transparent conducting TiO2 systems. *Hyomen Kagaku* **31,** 343–351 (2010).
13. Lin, P.-A., Jeng, H.-T. & Hsue, C.-S. Electronic structure and orbital ordering of $SrRu_{1-x}Ti_xO_3$: GGA+*U* Investigations. *Phys. Rev. B* **77,** 085118 (2008).
14. Kanoun, M. B., Goumri-Said, S., Schwingenschlogl, U. & Manchon, A. Magnetism in Sc-doped ZnO with zinc vacancies: A hybrid density functional and GGA+U approaches. *Chem. Phys. Lett.* **532,** 96–99 (2012).




DISTRIBUTION A: Distribution approved for public release

15. Morgan, B. J. & Watson, G. W. A DFT+U description of oxygen vacancies at the TiO2 rutile (110) surface. *Surf. Sci.* **601,** 5034–5041 (2007).
16. Scanlon, D. O., Walsh, A., Morgan, B. J. & Watson, G. W. An ab initio Study of Reduction of V2O5 through the Formation of Oxygen Vacancies and Li Intercalation. *J. Phys. Chem. C* **112,** 9903–9911 (2008).
17. Feng, J., Shian, S., Xiao, B. & Clarke, D. R. First-principles calculations of the high-temperature phase transformation in yttrium tantalate. *Phys. Rev. B* **90,** 1–13 (2014).
18. Huang, G. Y., Wang, C. Y. & Wang, J. T. Detailed check of the LDA+U and GGA+U corrected method for defect calculations in wurtzite ZnO. *Comput. Phys. Commun.* **183,** 1749–1752 (2012).
19. Wang, L., Maxisch, T. & Ceder, G. Oxidation energies of transition metal oxides within the GGA+U framework. *Phys. Rev. B* **73,** 195107 (2006).
20. Seo, D. *et al.* The structural and chemical origin of the oxygen redox activity in layered and cation-disordered Li-excess cathode materials. *Nat. Chem.* **8,** 692–697 (2016).
21. Saubanere, M., McCalla, E., Tarascon, J.-M. & Doublet, M.-L. The intriguing question of anionic redox in high-energy density cathodes for Li-ion batteries. *Energy Environ. Sci.* **9,** 984–991 (2016).
22. Zang, Y., Ding, C.-X., Wang, X.-C., Wen, Z.-Y. & Chen, C.-H. Molybdenum-doped lithium-rich layered-structured cathode material $Li_{1.2}Ni_{0.2}Mn_{0.6}O_2$ with high specific capacity and improved rate performance. *Electrochim. Acta* **168,** 234–239 (2015).
23. Qiu, B. *et al.* Gas-solid interfacial modification of oxygen activity in layered oxide cathodes for lithium-ion batteries. *Nat. Commun.* **7,** 12108 (2016).
24. Deng, X. *et al.* Selective Thermal Reduction of Single-layer $MoO_3$ nanostructures on Au(111) Selective Thermal Reduction of Single-layer $MoO_3$ nanostructures on Au(111). *Surf. Sci.* **602,** 1166–1174 (2007).
25. Ma, J. *et al.* Molybdenum Substitution for Improving the Charge Compensation and Activity of $Li_2MnO_3$. *Chem. - A Eur. J.* **20,** 8723–8730 (2014).
26. Kong, F. *et al.* Ab initio study of doping effects on LiMnO2 and Li2MnO3 cathode materials for Li-ion batteries. *J. Mater. Chem. A* **3,** 8489–8500 (2015).
27. Gao, Y. *et al.* Improved electron/Li-ion transport and oxygen stability of Mo-doped Li2MnO3. *J. Mater. Chem. A* **2,** 4811–4818 (2014).
28. Williams, D. B. & Carter, C. B. *Transmission Electron Microscopy: A Textbook for Materials Science*. *Materials Science* **1–4,** (2009).
29. Fell, C. R. *et al.* Correlation between oxygen vacancy, microstrain, and cation distribution in lithium-excess layered oxides during the first electrochemical cycle. *Chem. Mater.* **25,** 1621–1629 (2013).
30. Qian, D. *et al.* Lithium lanthanum titanium oxides: A fast ionic conductive coating for lithium-ion battery cathodes. *Chem. Mater.* **24,** 2744–2751 (2012).
31. Liu, H. *et al.* Communication—Enhancing the Electrochemical Performance of Lithium-Excess Layered Oxide $Li_{1.13}Ni_{0.3}Mn_{0.57}O_2$ via a Facile Nanoscale Surface Modification. *J. Electrochem. Soc.* **163,** A971–A973 (2016).
32. Qiu, B. *et al.* Enhanced Electrochemical Performance with Surface Coating by Reactive Magnetron Sputtering on Lithium-Rich Layered Oxide Electrodes. *ACS Appl. Mater. Interfaces* **6,** 9185–9193 (2014).
33. Li, J., Shunmugasundaram, R., Doig, R. & Dahn, J. R. In Situ X-ray Diffraction Study of Layered Li-Ni-Mn-Co Oxides: Effect of Particle Size and Structural Stability of Core-Shell Materials. *Chem. Mater.* **28,** 162–171 (2016).

**List of Publications and Significant Collaborations that resulted from your AOARD supported project:**

Ying Shirley Meng, "Enabling High Energy Long Life Rechargeable Batteries by Advanced Materials Diagnosis and *Operando* Characterization", **Keynote talk**, 2018 NSYSU-UCSD Bilateral Research Symposium, Kaohsiung, Taiwan, March 2018.



DISTRIBUTION A: Distribution approved for public release

Thomas A. Wynn*, Chengcheng Fang, Minghao Zhang, Haodong Liu, Daniel M. Davies, Ying Shirley Meng, "Defect-driven degradation mechanisms in Li-rich cathode materials", poster at the International Meeting on Lithium Batteries, Kyoto, Japan, June 2018.

Thomas A. Wynn*, Chengcheng Fang, Minghao Zhang, Haodong Liu, Daniel M. Davies, Ying Shirley Meng, "Computationally driven oxygen stabilization by cation substitution in lithium-rich cathode materials", oral presentation at the 231st Meeting of the Electrochemical Society, New Orleans, LA, May 2017.

Thomas A. Wynn, Chengcheng Fang, Minghao Zhang, Haodong Liu, Daniel Davies, Xuefeng Wang, Derek Lau, Jungwoo Z. Lee, Bo-Yuan Huang, Kuan-Zong Fung, Chung-Ta Ni, Ying Shirley Meng, "Mitigating oxygen release in anionic-redox-active cathode materials by cationic substitution through rational design", in peer review, second round 2018.

Collaborations on Li rich layered oxides – we have discovered anion redox activities in this class of materials. Doping and morphology control have significant effects on the anion redox activities and on how to control the voltage fading issues in this class of materials. Beside the collaboration with the Taiwan co-PI Dr. Fung, we are collaborating with Prof. Oleg Shpyrko (Physics) at UC San Diego to further explore the role of defects in this type of materials.



DISTRIBUTION A: Distribution approved for public release

# AFOSR Deliverables Submission Survey

Response ID:10210 Data

1.

**Report Type**

Final Report

**Primary Contact Email**

**Contact email if there is a problem with the report.**

shirleymeng@ucsd.edu

**Primary Contact Phone Number**

**Contact phone number if there is a problem with the report**

8579283689

**Organization / Institution name**

UC San Diego

**Grant/Contract Title**

**The full title of the funded effort.**

Development of advanced Li-rich xLi2MO3-(1-x)LiMO2 composite cathode for Li ion batteries with high energy density

**Grant/Contract Number**

**AFOSR assigned control number. It must begin with "FA9550" or "F49620" or "FA2386".**

FA2386-15-1-4110

**Principal Investigator Name**

**The full name of the principal investigator on the grant or contract.**

Ying Shirley Meng

**Program Officer**

**The AFOSR Program Officer currently assigned to the award**

Dr. Sheena Winder

**Reporting Period Start Date**

09/28/2015

**Reporting Period End Date**

05/27/2018

**Abstract**

Li-rich layered oxides (LRLO) composite cathode materials were studied with the goal of improving energy density with three main thrusts: computational modeling of cation substitution for stabilize oxygen, (2) exploration of coatings for improved capacity retention, and (3) mesostructural modification to improve cycling performance and rate capability. Computational modelling using density functional theory predicts 4d transition metals Mo and Ru to improve oxygen stability; experimental doping results were commensurate with calculation results, with Mo showed improved capacity retention and reduced oxygen evolution. LLTO coating was demonstrated to improve capacity retention by preventing surface reconstruction, as evident by high resolution scanning transmission electron microscopy. Mesostructure modification was explored through varied processing method, showing a high degree of particle tunability through precise processing control; such altered nanostructuring of secondary particles was shown to have a notable influence on particle cyclability.

Great progress was made to determine causes of structural instability and to mitigate such instabilities in

LRLO. Doping of a model layered Li-rich nickel manganese material was investigated via DFT calculations to explore stabilization of oxygen ions in the material, and guided by results, experimental doping and characterization was performed. The theoretical model was validated, as compared to previously published work on the evolution of oxygen vacancies. Of all dopants simulated, Mo and Ru were shown to increase the oxygen vacancy formation energy, EFOv, elucidating the potential to reduce oxygen evolution during cycling and improving overall capacity retention. This improved EFOv was attributed to a delocalization of the Mo electrons to the surrounding anions, serving to stabilize the oxygen ions by creating a larger barrier for charge transfer. Beyond pure understanding of the effect of dopants on the EFOv this work uncovered fundamental characteristics of degradation mechanisms within this class of materials.

**Distribution Statement**

**This is block 12 on the SF298 form.**

Distribution A - Approved for Public Release

**Explanation for Distribution Statement**

**If this is not approved for public release, please provide a short explanation. E.g., contains proprietary information.**

**SF298 Form**

**Please attach your SF298 form. A blank SF298 can be found here. Please do not password protect or secure the PDF**
**The maximum file size for an SF298 is 50MB.**

img-730120603-0001.pdf

**Upload the Report Document. File must be a PDF. Please do not password protect or secure the PDF . The maximum file size for the Report Document is 50MB.**

YMENG_Final_Performance_Report_2018.pdf
JMCA_Proof.pdf

**Upload a Report Document, if any. The maximum file size for the Report Document is 50MB.**

**Archival Publications (published) during reporting period:**

Thomas A. Wynn, Chengcheng Fang, Minghao Zhang, Haodong Liu, Daniel Davies, Xuefeng Wang, Derek Lau, Jungwoo Z. Lee, Bo-Yuan Huang, Kuan-Zong Fung, Chung-Ta Ni, Ying Shirley Meng, "Mitigating oxygen release in anionic-redox-active cathode materials by cationic substitution through rational design", in peer review, second round 2018.

**New discoveries, inventions, or patent disclosures:**
**Do you have any discoveries, inventions, or patent disclosures to report for this period?**

No

**Please describe and include any notable dates**

**Do you plan to pursue a claim for personal or organizational intellectual property?**

**Changes in research objectives (if any):**

None

**Change in AFOSR Program Officer, if any:**

Yes
Previous Program Officer - Dr. Kenneth Caster

**Extensions granted or milestones slipped, if any:**

None

**AFOSR LRIR Number**

**LRIR Title**

**Reporting Period**

**Laboratory Task Manager**

**Program Officer**

**Research Objectives**

**Technical Summary**

**Funding Summary by Cost Category (by FY, $K)**

| | Starting FY | FY+1 | FY+2 |
|---|---|---|---|
| Salary | | | |
| Equipment/Facilities | | | |
| Supplies | | | |
| Total | | | |

**Report Document**

image.png
image.png
image.png
image.png

**Report Document - Text Analysis**

**Report Document - Text Analysis**

**Appendix Documents**

image.png
image.png
image.png
image.png

## 2. Thank You

**E-mail user**

Aug 14, 2018 20:58:18 Success: Email Sent to: shirleymeng@ucsd.edu